Dragos, Jonathon; Wu, Chengqing; Haskett, Matthew Henry Thomas; Oehlers, Deric John
Derivation of normalized pressure impulse curves for flexural ultra high performance concrete slabs
Journal of Structural Engineering-ASCE, 2013; 139(6):875-885

Derivation of Normalized Pressure Impulse Curves for Flexural Ultra High Performance Concrete Slabs

[1]Jonathon Dragos, [2]Chengqing Wu, [3]Matthew Haskett and [4]Deric Oehlers

Abstract

In previous studies, a finite difference procedure has been developed to analyze the dynamic response of simply supported normal reinforced concrete (NRC) slabs under blast loads. Ultra high performance concrete (UHPC) is a relatively new material with high strength and high deformation capacity in comparison to conventional normal strength concrete. Therefore, the finite difference procedure for analysis of conventional reinforced concrete members against blast loads needs to be significantly adapted and extended to accommodate UHPC. In this paper, an advanced moment-rotation analysis model, employed to simulate the behavior of the plastic hinge of a UHPC member, is incorporated into the finite difference procedure for the dynamic response analysis of reinforced UHPC slabs under blast loads. The accuracy of the finite difference analysis model which utilized the moment-rotation analysis technique was validated using results from blast tests conducted on UHPC slabs. The validated finite difference model was then used to generate pressure impulse (PI) curves. Parametric studies were then conducted to investigate the effects of various sectional and member properties on PI curves. Based on the simulated results, two equations were derived which can be used to normalize a PI curve. Further numerical testing of the normalization equations for UHPC members was then undertaken. The generated normalized PI curve, accompanied by the derived normalization equations, can be used for the purposes of general UHPC blast design.

Introduction

The protection of structures against explosive loading is of growing importance for engineering communities and government agencies due to recent terrorist attacks (Luccioni et al. 2004; Thompson et al. 2004; Osteraas 2006; Islam and Yazdani 2008). Ultra high performance concrete (UHPC) is a relatively new construction material that is of high

[1]PhD student, School of Civil, Environmental and Mining Engineering, The University of Adelaide, SA 5005, Australia. Email: jdragos@civeng.adelaide.edu.au.
[2]Senior Lecturer, School of Civil, Environmental and Mining Engineering, The University of Adelaide, SA 5005, Australia. Email: cwu@civeng.adelaide.edu.au.
[3]Research Associate, School of Civil, Environmental and Mining Engineering, The University of Adelaide, SA 5005, Australia. Email: mhaskett@civeng.adelaide.edu.au.
[4]Professor, School of Civil, Environmental and Mining Engineering, The University of Adelaide, SA 5005, Australia. Email: doehlers@civeng.adelaide.edu.au.

strength, deformation capacity and toughness in comparison to conventional concrete. The superior strength and ductility of UHPC endows it with the ability to absorb remarkable amounts of energy before failure, making it a material suitable for the construction of military structures and strategically important buildings as protection against blast and impact loading (Gupta et al. 2005; Luo et al. 2007; Ngo et al. 2007; Wu et al. 2009a). Although experimental studies have been conducted on blast resistance of UHPC members (Wu et al. 2009a), surprisingly little research has been conducted to investigate its dynamic performance under blast loads numerically and analytically. Due to the significant difference in mechanical properties of UHPC, conventional analytical methods, such as single degree of freedom, finite difference and finite element models, need to be extended to accommodate UHPC. It has been proven that the finite difference analysis method is an accurate and fast running method suitable for the prediction of the behavior of normal reinforced concrete (NRC) members subjected to high intensity, short duration dynamic loads such as those associated with impacts and explosions (Krauthammer et al. 1993, 1994; Jones et al. 2009). It is expected that the finite difference model can also be used for the dynamic analysis of UHPC members subjected to blast loads.

The finite difference (FD) model incorporates the variation of blast loading distribution and mechanical properties of the cross section along the member, and accommodates shear and flexural deformations with strain rate effects. Such a model has been developed by Jones et al. (2009) to predict the behavior of NRC members subjected to blast and impulsive loading. Within this FD model, a moment-curvature relationship, determined assuming full interaction between the steel bar and concrete, is utilized for NRC members. When analyzing a RC beam in flexure, once the elastic limit is reached, it is assumed that a plastic hinge region forms in which a large amount of rotation occurs over a discrete region, known as the hinge length. The hinge length is determined empirically and there is no general agreement on the value or even which parameters to use to find the hinge length (Haskett et al. 2009). Traditionally, the rotation is found by multiplying the hinge length by the curvature obtained from the moment-curvature relationship and, due to this, is deemed only to be an empirical method. Recently, an advanced mechanics based approach was developed by Haskett et al. (2009) to determine the rotation of a NRC section taking into account the slip characteristics of the reinforcing steel and the softening wedge of concrete. Based on this, it is possible to derive a more accurate moment-rotation relationship for the plastic hinge of a NRC member. However, due to the addition of small steel fibers into the UHPC mix, while NRC is assumed to have no tensile strength in analyses, UHPC has a flexural tensile strength of approximately 30 MPa. To accommodate such differences, the moment-rotation model developed for NRC members by Haskett et al. (2009) needs to be extended for UHPC members.

Currently, pressure impulse (PI) diagrams based on the equivalent single degree of freedom (SDOF) approach and numerical approaches have been adopted for use during building design in order to assess the effects of blasts on structures (UFC-3-340-02 2008; Fallah and Louca 2007; Shi et al. 2008). Fallah and Louca (2007) derived analytical formulae (quasi-static and impulsive asymptotes) which can be used to determine a normalized PI diagram. The formulae are based on a SDOF system with a bi-linear resistance deflection curve, i.e. elastic-plastic hardening, elastic-plastic softening or elastic-perfectly plastic. Although the use of the bi-linear resistance deflection curve is more appropriate, the SDOF model can not consider a spatially and temporally varying distribution of blast loading, and is incapable of allowing for variations of mechanical properties of the cross section along the member. Shi et al. (2008) attempted to derive analytical formulae which can be used to derive a normalized PI diagram for reinforced concrete (RC) columns. The analytical formulae are functions of the properties of the member, such as reinforcing ratio and depth of the member. The formulae are limited by the small range of parameters which were investigated in the parametric study. For example, the effects of steel bars with strain hardening properties and also the effects of higher strength (above 50MPa) concretes were not investigated. Therefore, the PI diagram and the analytical formulae presented by Shi et al. (2008) cannot be used for a UHPC member, or for a member containing steel bars which are not perfectly elastic-plastic. Also, to apply the formulae, the conditions of the parametric study which were held constant, such as cover and reinforcing bar placement, must be replicated.

In this study, the finite difference model for NRC members is extended to accommodate UHPC members by incorporating the properties of the blast load and the advanced moment-rotation model into the analysis. The extended finite difference model is validated using data from blast tests conducted on UHPC members. With the validated finite difference model, parametric studies are carried out to derive PI diagrams, which have been widely used in the design of conventional RC structures against blast loads, for UHPC members. Using the simulated results, two equations, which can be used to normalize a PI curve for a UHPC member, have been identified and tested. A normalized PI curve has been derived which, when accompanied by the two normalization equations, can be used for the generic assessment of structures to establish safe response limits for given blast loading scenarios.

Moment-rotation analysis of UHPC members

A novel approach to incorporate the uncracked tension force of UHPC, steel fibers and steel forces in the cracked section, and a softening wedge in the compression zone into the rigid body rotation analysis developed by Haskett et al. (2009), as shown in Figure 1, was developed to determine the moment-rotation relationship for UHPC members by Dragos et al. (2010). The steel fibers are responsible for a significant increase in the tensile strength of UHPC. The tensile force contributed by the fibers in UHPC is obtained through an experimental stress-crack width relationship by Jungwirth and Muttoni (2004) using a slice approach. This approach, usually referred to as the layered capacity method (Wu et al. 2009b), involves splitting the cracked tensile zone, as seen in Figure 1, into thin horizontal slices. Each slice has a given crack width, and thus has a given stress which can be determined using the above mentioned stress-crack width relationship. For each slice, these stresses can then be converted to forces which contribute to the overall moment. To incorporate an uncracked and cracked tensile force, due to the steel fibers, the method developed by Haskett et al. (2009) had to be modified by assuming a linear strain profile. This allowed the model to determine a moment-rotation relationship and a moment-curvature relationship for a given section. The incorporation of steel fibers within this type of analysis enabled more accurate moment-rotation curves to be determined.

The new model was divided into four stages to incorporate the uncracked tension force of UHPC, effects of steel fibers, steel forces in the cracked section and softening wedge in the compression zone. The four stages are Stage 1: Prior to cracking; Stage 2: Crack below the reinforcement; Stage 3: Before formation of softening wedge; and Stage 4: After formation of softening wedge. In stage 1, since the tensile region is uncracked, all forces in the compressive and tensile region can be obtained by the assumption of a linear strain profile. The curvature and moment can be obtained by achieving force equilibrium. In stage 2, when a crack forms below the reinforcement, additional forces within this cracked region due to the steel fibers in the cracked section are calculated based on the stress-crack width relationship. All other forces are obtained based on the linear strain profile assumption as above. Now that a crack has formed, a moment, curvature and a rotation can be determined for this stage and all subsequent stages. In stage 3, the crack apex is above the steel reinforcement, therefore a slip exists between the steel reinforcement and the concrete on the inside crack face, denoted by s_{reinf} in Figure 1. Partial interaction theory is used to determine the tension force of steel reinforcement based on a given slip. The partial interaction model, developed by Haskett et al. (2007), is the method in which a local bond stress strain relationship, between the steel reinforcement and concrete, is used to determine a global load slip relationship. A bi-linear bond slip relationship was adopted and equations, based on this, were derived for the load slip relationship by Muhamad et al. (2010) and used in the analysis. The same procedures as in stage 2 are used to determine all other forces. Stage 3 ends when the strain in the top fiber of the slab reaches the crushing strain. In stage 4, a softening wedge forms as the strain in the top fiber of the slab has exceeded the crushing strain. In this stage, the concrete compressive force is divided into two parts. The first is the ascending region, which is calculated using Hognestad's concrete stress-strain model and acts below the wedge. The second is the softening force due to the formation of the softening wedge. The rest of the forces are calculated using the procedures discussed in stage 3. In any stage, the analysis stops when bar fracture, bar debonding or wedge failure occurs.

The moment-rotation analysis was used to determine a moment-curvature and moment-rotation relationship for slab D2B, which was used in the 2008 static test program. The 2008 static test program, by Ciccarelli et al. (2008), consisted of two-point bending tests of 2 UHPC slabs (D2B and D3B) resting on simple supports. It also consisted of compression tests of UHPC cylinders which were utilized to assure the suitability of using Hognestad's concrete stress-strain model for the ascending portion of the compression region for UHPC members. Parameters for the compressive behavior of UHPC were obtained from the cylinder tests, where as all other parameters were provided by the manufacturer. The reinforced UHPC slab, D2B, has a span of 2000mm, width of 1000mm and a thickness of 100mm. It is reinforced with a 12.7mm diameter mild steel mesh with yield strength of 600 MPa that is spaced at 100mm centers in the major bending plane (0.8%) and at 200mm centers in the minor plane. The UHPC had an average compressive strength of 175 MPa, tensile capacity of 22 MPa and Young's modulus of 47 GPa. The moment-curvature and moment-rotation relationships were used to derive a theoretical load deflection relationship which was compared to the experimental load deflection relationship of slab D2B in Figure 2.

Although the dynamic response model as a whole is primarily interested in the behavior of

UHPC members at or near ultimate state, Figure 2 helps to justify why it is worth modelling the sectional behavior at the early stages of cracking. For a NRC section, cracking typically occurs at a very low moment. However, for a UHPC section, cracking occurs at a moment which can be up to 70% of its ultimate moment capacity. This is due to the addition of fibers in the UHPC material, which causes the material to have a significantly larger tensile strength which cannot be ignored. This can be seen in Figure 2 as the horizontal portion, at approximately 250kN, represents the point at which cracking occurs. As this region influences the dynamic behavior of members against large blasts which cause failure, it is deemed important to model this region more accurately. From Figure 2, it can be seen that there are large discrepancies between the theoretical and experimental curves in the rising branch, shown by the horizontal arrow, but the results are much more reasonable at ultimate conditions. As the stress-crack width relationship determined by Jungwirth and Muttoni (2004) was used, this is attributed to the difference in material properties between the UHPC material used in this study and that used in their study. Therefore, the deflections caused by larger loads are quite accurate, whereas the deflections caused by smaller loads are not as accurate. The above moment-rotation analysis model provides moment-curvature and moment-rotation relationships which are inputs for the finite difference model for determining the dynamic response of UHPC members against blast loads. Although the model is not fully accurate, what is most important is the concept of modelling the response of the plastic hinge via a moment-rotation relationship in a dynamic model.

Finite difference analysis of UHPC members

The Timoshenko Beam Theory (Weaver and Timoshenko 1990) accounts for shear deformation and rotational inertia, being solved for in the FD model. The dynamic equilibrium equations are as follows:

$$\frac{\partial M}{\partial x} - Q = -\rho_m I \frac{\partial^2 \beta}{\partial t^2} \tag{1}$$

$$\frac{\partial Q}{\partial x} + q + P_a \frac{\partial \beta}{\partial x} = \rho_m A \frac{\partial^2 v}{\partial t^2} \tag{2}$$

Where: M = bending moment, Q = shear force, q = load acting transverse to the beam, P_a = axial load in the beam, A = cross sectional area, I = moment of inertia of the beam, ρ_m = mass density of the beam, β = rotation and v = transverse displacement.

Numerical method

The response of the member is determined using the finite difference method. The numerical techniques were redeveloped from that of Ciccarelli et al. (2008), which were extensions from the work on Krauthammer et al. (1993). Equations 3 and 4 show how the rotation and displacement, respectively, of node i at time $t + 1$ are calculated.

$$\beta_i^{t+1} = 2\beta_i^t - \beta_i^{t-1} - \frac{dt^2}{\rho_m I_i}\left[\frac{M_{i+1}^t - M_{i-1}^t}{2dx} - Q(i)\right] \tag{3}$$

$$v_i^{t+1} = 2v_i^t - v_i^{t-1} + \frac{dt^2}{\rho_m A_i}\left[\frac{Q_{i+1}^t - Q_{i-1}^t}{2dx} + q(i)\right] \tag{4}$$

To calculate the rotation and displacement for the new timestep using equations 3 and 4, respectively, the shear force at each node must be known. The shear force at each node is calculated as a function of shear strain. The shear strain, seen in equation 5, is calculated by converting the partial derivative into finite difference form (Krauthammer et al. 1993).

$$\gamma_{xz\,i}^{\ t} = \frac{\partial v}{\partial x} - \beta = \frac{v_{i+1}^t - v_{i-1}^t}{2dx} - \beta_i^t \tag{5}$$

To calculate the rotation for the new timestep using equation 3, the bending moment at each node must be known. At the non plastic hinge regions, the bending moment of a node is calculated as a function of curvature using the moment-curvature relationship. At the plastic hinge region, the bending moment of a node is calculated as a function of its rotation using the moment-rotation relationship. The moment-curvature relationship and moment-rotation relationship of a member are both derived using the moment-rotation model. The curvature, seen in equation 6, is also calculated by converting the partial derivative into finite difference form (Krauthammer et al. 1993).

$$\phi_i^t = -\frac{\partial \beta}{\partial x} = -\frac{\beta_{i+1}^t - \beta_{i-1}^t}{2dx} \tag{6}$$

The plastic hinge region was modeled in such a way that the discrete rotation of the plastic hinge occurred between two adjacent nodes. Therefore, by knowing the rotation of the adjacent nodes, β_{left}^{t} and β_{right}^{t}, the discrete rotation of the plastic hinge, as defined by Haskett et al. (2009), can be calculated and can be seen in equation 7.

$$\theta_i^t = -\frac{\beta_{right}^t - \beta_{left}^t}{2} \tag{7}$$

It is important to note that modelling of the plastic hinge begins at the onset of cracking of a particular node. This was done by calculating the curvature in which cracking occurs, so that when the curvature of the node reaches the cracking curvature, moment-rotation is then used to model that region as a plastic hinge. A plastic hinge was assumed to only form at the center for a simply supported member, and they were assumed to form at the ends and the center for a member fixed at both supports.

The finite difference method allows an arbitrary blast load to be applied on each node of the member as a function of time. This allows one to determine the structural response of a member due to a pressure history which has been derived by codes, equations or measured directly through experiments. However, due to the assumption of the positions in which the plastic hinges form, only blast loads which are symmetrical about the midspan can be applied.

Shear behavior

Linear shear stress strain theory was used to calculate the shear force, Q, from the shear strain, as can be seen in equation 8.

$$Q = KA\sigma_{xz} = KAG\gamma_{xz} \tag{8}$$

Where: G = shear stiffness, σ_{xz} = shear stress, γ_{xz} = shear strain and K = correction factor which is used to take into account the constant cross sectional shear stress assumption. $K = \pi^2/12$ for rectangular cross sections, as given by Krauthammer et al. (1993).

Validation of structural response model

The model developed by Jones et al. (2009) successfully predicted the response of NRC slabs subjected to external blast loads. Therefore, the validation of UHPC slabs under external blast loads was the main focus of this section. As can be seen in Table 1, two blast events involving UHPC slabs with a span of 2000mm, 1000mm wide and 100mm thick were chosen for validation; events 6 and 7 (Ciccarelli et al. 2008). During event 6, slab D2B was subjected to a blast from a cylindrical charge, whereas during event 7, slab D3B was subjected to a blast from a cylindrical charge. Both cylindrical charges were oriented in the radial direction, meaning the primary axis of the cylindrical charge was directed parallel to the plane of the slab. No overpressure history data was obtained from these tests, so they had to be estimated from the research done by Burge et al. (2009). This involved converting the peak reflected overpressure and impulse predicted by UFC guidelines (UFC-3-340-02 2008) for a spherical charge to that of a cylindrical charge of the same scaled distance in the radial direction. It should be emphasized that the predicted pressure history will have a significant influence on the results, so should be considered when evaluating the suitability of the structural response model.

During the validation process, it had to be decided whether to model the response under pinned or fixed end support conditions. From the blast tests, Ciccarelli et al. (2008) observed that the end restraints, which each consisted of two steel equal angles bolted together to act as a clamp, could not be considered to be fully fixed or fully pinned. They witnessed that for large blasts, which caused large deflections, the clamps would give way, but for small blasts, causing small deflections, the clamps would remain fully intact. Therefore, it was deduced that when the moment developed at the ends of the slab was believed to be large, due to a large blast causing large deflections, the restraint could be considered pinned. Conversely, for small developed moments at the ends of the slab, due to small blasts causing small deflections, fixed end conditions could be considered more suitable. For each blast event, this was how the end support conditions were chosen during validation.

Figure 3 shows the deflection history for event 6. This response is of slab D2B subjected to a blast with a small scaled distance, which caused the member to collapse. The model correctly predicts that the member fails. It also roughly estimates at what time and deflection collapse of the member occurs. The discrepancy due to the increased initial stiffness of the theoretically developed moment-curvature relationship can be observed, as the theoretical deflection at failure occurs earlier than the experimental deflection at failure.

Figure 4 shows the deflection history for event 7. This is the response of slab D3B under a charge which caused a significant deflection. It can be seen that the model reasonably predicts the maximum deflection in this case. The discrepancy in the time to reach the maximum deflection can be accredited to the increased initial stiffness of the theoretically developed moment-curvature and moment-rotation relationships of slab D3B. The discrepancy in the falling branch can not only be described by the increased initial stiffness, but also because of the fact that the structural response model does not attempt to model the post peak behavior of the member response. Therefore, the unloading curve of the member response may not be correct. The correct post peak behavior was not modeled as only the first peak of the deflection history was required for this research and because modeling of the post peak response can be very difficult.

After observing Figure 3 and Figure 4, it can be seen that for larger blast loads, and thus larger deflections, the differences in the results are quite small. This is because the inaccuracy of the moment-rotation model in the elastic region, before cracking occurs, has a negligible effect on the response of structural members near ultimate state. As this research is more interested in the response of structural members under large blasts, which cause large deflections, the model was considered to be appropriate.

Overpressure impulse curve

Blast loads can cause failure at various combinations of peak reflected pressure and impulse. A PI curve is the envelope of all overpressure histories, plotted on axes of impulse and peak reflected overpressure, which cause failure. The PI curve can be used as a tool to design members against blast loads, if the peak reflected overpressure and impulse of the blast are known.

PI curve generation

The structural response model was extended from that of Ciccarelli et al. (2008) to then determine the PI curve of a given member. This was possible because the moment-rotation model could accurately predict the rotation at which failure occurred. This ultimate rotation of the plastic hinge was then used as the failure criteria. The PI curve developed for slab D3B can be seen in Figure 5. To generate a PI curve, the minimum peak reflected overpressure and a very large impulse, altered by manipulating t_d, had to be chosen. They had to be chosen such that it was known those two parameters for a particular blast load would cause failure for the given member. The program then decreases the impulse, by decreasing t_d, without changing P_r and runs the structural response simulation. This process is iterated until it is found that the member survives a simulation. The peak reflected overpressure and impulse of this particular overpressure history is then plotted on the PI diagram axes. The peak reflected overpressure is then increased, which in turn also increases the impulse of the blast load as t_d is not changed. For example, in Figure 5, if point B was known, to find the next point on the PI curve, the structural response model would first increase P_r without changing t_d, seen as arrow 1. Then it would incrementally reduce the impulse, seen as arrows 2, 3 and 4, until point C has been located. That is the next point in which the member survives a simulation. The above process is repeated such that many points are plotted on the PI diagram. These points then form the PI curve.

Figure 5 shows how for large impulses, the peak reflected overpressure of the PI curve converges to a minimum value, P_{rmin}. It also shows that for large peak reflected overpressures, the impulse of the PI curve converges to a minimum value, I_{min}. Finally, between these extremes lies a transition zone, for example point C. A blast load which lies in the lower right hand side of the PI diagram, for example point A in Figure 5, can be thought of as an explosion from a large charge weight and a large standoff distance. This is because such a blast will cause a pressure history with a small peak reflected overpressure, a large duration, t_d, and also a large impulse. Conversely, a blast load which lies in the upper left hand side of the PI diagram, for example point D in Figure 5, can be thought of as an explosion from a small charge weight but a small standoff distance. This is because such a blast will cause a pressure history with a large peak reflected overpressure, a small duration, t_d, and also a small impulse. Figure 5 also displays the safe zone and failure zone of the PI curve of slab D3B, which shows whether the member will fail or survive under any given external blast load. The structural response model assumes that the overpressure history is uniformly distributed on the slab. Therefore, the effects of angles of incidence along the slab are ignored, and the effects of time of arrival differences along the slab are also ignored. As the angle of incidence increases, the pressure history typically becomes less damaging. Therefore, as long as the maximum pressure history is assumed to act on the entire slab, the developed PI curve can be thought of as conservative.

Normalization of PI curves

The structural response model can be used to generate PI curves for a given member for collapse. Using this data, the normalization of PI curves will take place. This includes understanding what factors affect the PI curve of given members so that empirical equations of proportionality or empirical normalization equations, for slabs with pinned supports, can be developed. This allows the designer to quickly draw a PI curve based on the member and sectional properties of the slab.

Methodology

The effects of member and sectional properties on PI curves were investigated. The member properties investigated included span and depth whereas the sectional property investigated was the moment-rotation relationship. As this study only applies to one-way slabs, the effects of the width of the slab on the PI curve were not investigated as the width of a one-way spanning slab has no effect on its response.

To normalize the PI curves the effects of member and sectional properties on the minimum impulse, I_{min}, and minimum peak reflected overpressure, P_{rmin}, asymptotes were studied. Therefore, the concept of a control specimen had to be introduced. When manipulating a property, for example the span of the member, the asymptotes had to be factored up or down from that of the control specimen to understand how it affected P_{rmin} and I_{min}. It should be noted that the aim of this section is to determine equations for P_{rmin} and I_{min} only. Any PI curve, with asymptotes of unity, can be used in conjunction with the equations developed in this study to determine the PI curve of a given member.

Span of a member

To normalize the span of a member, a section with a certain width, depth and moment-rotation relationship was chosen. The span was then altered to find the effects of this parameter on P_{rmin} and I_{min}. PI curves for slabs of varying spans can be seen in Figure 6. From Figure 6, P_{rmin} and I_{min} values can be determined for each span. The ratio of these 2 values, for each span, to those of the control specimen ($P_{rmin,o}$ and $I_{min,o}$, respectively) can be plotted to find how the span affects the PI curve. In this case, the slab with length 1.78m is the control specimen. The plots can be seen in Figure 7 for P_{rmin} and I_{min}, respectively.

Figure 7(a) shows that P_{rmin} is inversely proportional to L^2. This is expected since a blast which is controlled by peak reflected overpressure is similar to that of a static uniformly distributed load, as it has a longer duration. For slabs with the same moment capacity subjected to static uniform overpressures, the overpressure capacity is also inversely proportional to L^2. Figure 7(b) shows that I_{min} is proportional to $L^{-0.25}$. This is different since other additional factors are affected by the slabs span, such as its total mass and its ability to absorb energy. These additional factors also affect the slab's ability to resist impulse controlled blasts.

Moment-rotation relationship

To understand how the shape of the moment-rotation relationship affected P_{rmin} and I_{min}, a control slab was chosen, and PI curves were determined for many slabs with moment-rotation relationships which differ from the control slab. All slabs contained UHPC, reinforced with high strength steel bars, with an ultimate strength of 1800MPa, in the tensile region only. To produce different moment-rotation relationships, the reinforcing ratio, from 1% to 3.5%, and bond stress characteristics between the steel bars and concrete were changed.

Using the structural response model, PI curves were determined for each of the slabs with differing moment-rotation relationships. From these PI curves, P_{rmin} and I_{min} were determined. The aim was then to develop equations which can be used to determine P_{rmin} and I_{min} based on any moment-rotation relationship. To do this, it was necessary to identify the main points on the moment-rotation relationship which affected P_{rmin} and I_{min}. As all moment-rotation relationships were of bi-linear shape, three values, corresponding to two points on the moment-rotation relationship, were recognized as having influence over P_{rmin} and I_{min}. These values were the ultimate moment (M_u), yield moment (M_y) and the ultimate rotation (θ_u).

When investigating the effects of the moment-rotation relationship on P_{rmin}, it was observed that P_{rmin} was proportional to the product of 3 terms. The first term is the ultimate moment which has the most influence over P_{rmin}. The other 2 terms were factors derived from the three influential moment-rotation relationship values. The two factors were named, Yield Factor (Pressure) (Eq. 9) and Dynamic Ductility Shape Factor (Eq. 10):

$$k_{yp} = \left({}^{M_y}/_{M_u} \right)^{0.293} \tag{9}$$

$$k_{duc} = \left({}^{\theta_u}/_{M_u} \right)^{0.168} \tag{10}$$

Therefore, if the control specimen was denoted with subscript “o”, the analyses resulted in the following:

$$\frac{P_{rmin}}{P_{rmin,o}} = \frac{k_{yp} k_{duc} M_u}{k_{yp,o} k_{duc,o} M_{u,o}} \tag{11}$$

The derivation of equations 9, 10 and 11 can be seen in Table 2. $k_{yp,power}$ and $k_{duc,power}$ represent the exponents used in k_{yp} and k_{duc}, respectively. The exponents were determined using a goal seek method to minimize the average of the absolute errors.

Using the same approach for P_{rmin}, I_{min} was found to be proportional to the square root of one term and inversely proportional to the square root of another term. The first term was named the Energy Absorption Capacity Factor (Eq. 12) and the second term was named the Yield Factor (impulse) (Eq. 13):

$$W = M_u \theta_u \tag{12}$$

$$k_{yi} = {}^{M_y}/_{M_u} \tag{13}$$

Similarly, denoting the control specimen with subscript “o”, the analyses resulted in the following:

$$\frac{I_{min}}{I_{min,o}} = \sqrt{\frac{W/k_{yi}}{W_o/k_{yi,o}}} \tag{14}$$

The derivation of equations 12, 13 and 14 can be seen in Table 3. $k_{yi,power}$ represents the exponent used in k_{yi}. This exponent was determined using a goal seek method to minimize the average of the absolute errors.

Finally, it was necessary to define ultimate moment, yield moment in such a way that the width of the slab had no effect on P_{rmin} and I_{min}. Therefore, M_u and M_y were defined as ultimate moment per unit width and yield moment per unit width, respectively.

Depth of a member

Manipulating the depth of a member affects both the moment-rotation relationship and the member's total mass. Therefore, it affects P_{rmin} and I_{min} both at the sectional and member level. When changing the depth of the slab, the cover to the center of the reinforcing bars was held constant, say 30mm. As the moment-rotation relationship for each depth was known, equations 11 and 14 were used to normalize P_{rmin} and I_{min}, respectively, at the sectional level. For both P_{rmin} and I_{min}, it was observed that further manipulation was required to normalize the PI curves based on depth. The results indicated that P_{rmin} was also proportional to $D^{0.586}$ and that I_{min} was also proportional to $D^{0.616}$. This additional proportionality is how the depth affects the PI curve at the member level, due to the addition of mass.

The effects of the depth of the member on P_{rmin} are quantified in Table 4. The exponent, $D_{p,power}$, was determined using a goal seek method to minimize the average of the absolute errors. In Table 4, columns 2, 3 and 4 represent the effects of the moment-rotation relationship which occurs when a change in depth is chosen. This had to be normalized before the effects of the depth could be determined.

The effects of the depth of the member on I_{min} are quantified in Table 5. The exponent, $D_{i,power}$, was determined using a goal seek method to minimize the average of the absolute errors. In Table 5, columns 2 and 3 show the effects of the moment-rotation relationship which occurs when a change in depth is selected. This had to be normalized before the effects of the depth could be determined.

Normalization equations

As the effects of the span, depth, width and moment-rotation relationship had been identified, they were then combined to produce normalization equations for P_{rmin} (Eq. 15) and I_{min} (Eq. 16).

$$\frac{P_{rmin}}{P_{rmin,o}} = \frac{k_{yp} k_{duc} D^{0.584} L^{-2} M_u}{k_{yp,o} k_{duc,o} {D_o}^{0.584} {L_o}^{-2} M_{u,o}} \tag{15}$$

$$\frac{I_{min}}{I_{min,o}} = \sqrt{\frac{W D^{1.231} L^{-0.5} / k_{yi}}{W_o {D_o}^{1.231} {L_o}^{-0.5} / k_{yi,o}}} \tag{16}$$

Equations 15 and 16 show that, if $P_{rmin,o}$ and $I_{min,o}$, and all the discussed parameters of the control specimen and the desired specimen are given, P_{rmin} and I_{min} for the desired specimen can be calculated. For all parameters used in Equations 15 and 16, any units can be used. However, the same units used for a parameter with a subscript "o" should also be used for its corresponding parameter without a subscript "o". The equations are valid for one way slabs with a span between 1m and 4m and a depth between 100mm and 240mm. Also, the equations are valid for an ultimate hinge rotation of less than 0.23rad or 13^{o}. This is significantly large considering that ASCE Guidelines (ASCE, 1997 & ASCE, 2008) suggest that 8^{o} is a high level of rotation. As the entire PI curve, for a typical RC slab subjected to an external blast, can be defined by P_{rmin} and I_{min}, this allows one to determine the PI curve for any desired RC slab, based on member and sectional properties, for the purpose of preliminary design. Although the equations are not completely based on structural dynamics principles, but are purely empirical, they can still be used to gain insight into how slabs resist various types of blast loads. Also, they can be used as a starting point for deriving normalization equations for PI curves based on structural dynamics principles.

To derive a normalized PI curve based on equations 15 and 16, a control specimen with a given I_{min} and P_{rmin} is required. The parameters of the control specimen are shown in Table 6. After substituting all the parameters of the control specimen into equations 15 and 16, a normalized PI curve, seen in Figure 8, with corresponding normalized PI curve equations, seen as Equations 17 and 18, can be developed. Due to the nature of Equations 15 and 16, the units used for parameters in Equations 17 and 18 should correspond with that used for the control specimen parameters, as shown in Table 6.

$$\rightarrow P_{rmin} = 1.80\left(k_{yp} k_{duc} D^{0.584} L^{-2} M_u\right) \tag{17}$$

$$\rightarrow I_{min} = 57.04\sqrt{W D^{1.231} L^{-0.5} / k_{yi}} \tag{18}$$

Equations 17 and 18 can be used in the normalized PI curve, shown in Figure 8, where the coordinates, P_r and I, should be scaled up by, P_{rmin} and I_{min} given above, respectively. The shape and equation of the normalized PI curve in Figure 8 is that of a typical RC slab subjected to an external blast load. This normalized PI curve can be replaced with any other normalized PI curve, with vertical and horizontal asymptotes of unity.

When studying the effects of sectional properties on P_{rmin} and I_{min}, it was observed that the cracking moment had very little effect on the results, therefore it was ignored. Also, the initial stiffness of the moment-curvature relationship was ignored as this would have very little effect on the structural response due to large blasts, causing nearly ultimate deflections. Also, although the Timoshenko Beam Equations take into account deflections due to shear using a linear shear stress strain relationship, the effects of shear properties were not considered in our investigation. This is because most span to depth ratios of conventional slabs, designed against blasts, range from 10 to 50, so the effects of shear properties were considered insignificant. However, it is known that, even for slabs with larger span to depth ratios, for large blasts with a small standoff distance, shear behavior can influence the response. This type of blast corresponds to the impulse controlled region of the PI diagram. Therefore, the use of the normalized PI curve for blasts within this region should only be used if it is known that shear behavior has no dominant influence on the response of the slab to such blasts. Also, this approach is not suitable for blasts with extremely small standoff distances as local damage of the slab can occur. This is because the structural response model can only simulate the global response of the member and not the local damage of the material itself due to concentrated effects of the blast.

Numerical testing of normalization equations

Although numerically derived results for many different slabs were used to produce the normalization equations, further numerical testing of the equations was undertaken. This was done by generating PI curves for slabs with varying depths and reinforcing ratios, using both the normalization equations and the structural response model, and comparing them. Figure 9 shows PI curves for 2 slabs which differ in depth and reinforcing ratio, in comparison to that of the control slab. It can be seen that the results are quite good as P_{rmin}, I_{min} and the transition zone match up quite well for both cases.

In the tests shown in Figure 9, the maximum error of the asymptotes, P_{rmin} and I_{min}, between the numerically derived results and that obtained through the normalization equations, is 5%. It can be seen that the instability within the structural response model can sometimes occur and can sometimes cause noticeable errors within the transition zone of the generated PI curves. However, it should be noted that the aim of this section is to only derive normalization equations for the asymptotes, P_{rmin} and I_{min}. It can be seen that at the extremes of the generated PI curves, towards P_{rmin} and I_{min}, the instability, which is represented by zig-zagging, decreases significantly. This is why the maximum errors experienced, when calculating P_{rmin} and I_{min}, are only 5%. These errors are attributed to the uncertainty involved in determining P_{rmin} and I_{min} for various UHPC slabs used to derive the normalization equations. Also, as a moment-rotation relationship is never exactly bilinear, the errors are also attributed to the judgment which should be used when determining the moment at yield, M_y.

Conclusion

An innovative approach was developed to predict the sectional behavior of a reinforced UHPC member accurately. The approach used modified rigid body analysis, curvature analysis and incorporated a stress-strain/crack width relationship to develop a new moment-rotation relationship. The moment-rotation and moment-curvature relationships were incorporated into a finite difference model which was validated using blast test data. With the validated finite difference model, the entire dynamic structural response model was recreated and also extended to generate PI curves. From an extensive parametric study, a normalized PI curve, accompanied by two equations for the asymptotes, were also derived. This was done by developing empirical equations of proportionality for various sectional and member properties, which can be used to generate a PI curve for any given member.

Acknowledgements

The financial and technical support of DSTO and VSL and the financial support of the Australian research Council under ARC Linkage Project LP 0883451 are gratefully acknowledged.

References

- American Society of Civil Engineers (ASCE). (1997). *Design of blast resistant buildings in petrochemical facilities*. Reston, VA.

- American Society of Civil Engineers (ASCE) (2008). *Blast Protection of Buildings*. Ballot version 2, Reston, VA.
- Burge, J., Carter, T., Fattori, G., & Miller, D. (2009). *Blast Resistance of Ultra High Performance Concrete.* Final Year Research Report, School of Civil and Environmental Engineering, The University of Adelaide, Australia.
- Ciccarelli, J., Henderson, A., Jordans, K., Noack, B., Oehlers, D., Wu, C. (2008). *Resistance Against Explosive Loading of Metal Foam Retrofitted and Ultra High Strength Concrete Structural Members.* Final Year Research Report, School of Civil and Environmental Engineering, The University of Adelaide, Australia.
- Dragos, J., Hu, Y., Lukazewicz, M., Ren, J. (2010). *Confined Blast-loading and Blast Resistance of Ultra-High Performance Concrete.* Final Year Research Project Report, School of Civil and Environmental Engineering, The University of Adelaide, Adelaide, Australia.
- Fallah, A.S., Louca, L.A. (2004).Pressure-impulse diagrams for elastic-plastic-hardening and softening single-degree-of-freedom models subjects to blast loading. *International Journal of Impact Engineering*, 34 (2007), 823-842.
- Gupta, A., Ngo, T., Lumantarna, R., Mendis, P., Cavill, B. (2005). Testing and modelling of ultra-high strength concrete panels subjected to blast and ballistic impact. *6th Asia-Pacific Conference on Shock & Impact Loads on Structures,* pg. 235 – 242
- Haskett, M., Oehlers, D.J., Ali, M.S.M. (2007). Local and global bond characteristics of steel reinforcement bars. *Engineering Structures*, 30 (2), 376-383.
- Haskett, M., Oehlers, D.J., Ali, M.S.M., Wu, C.Q. (2009). Rigid Body Moment-Rotation Mechanism for Reinforced Concrete Beam Hinges. *Engineering Structures*, 31 (5)1032-1041.
- Islam, A.K.M.A., Yazdani, N. (2008). Performance of AASHTO girder bridges under blast loading. *Engineering Structures*, 30 (7), 1922-1937.
- Jones, J., Wu, C., Oehlers, D.J., Whittaker, A.S., Marks, S., Coppola, R. (2009). Finite difference analysis of RC panels for blast effects. *Engineering Structures*, 31 (12), 2825-2832.
- Jungwirth, J., Muttoni, A. (2004). Structural Behaviour of Tension Members in UHPC. *Swiss Federal Institute of Technology (EPFL)*, Lausanne, Switzerland.

- Krauthammer, T., Shanaa, H., Assadi, A. (1994). Response of structural concrete elements to severe impulsive loads. *Computers and Structures*, 53 (1), 119-130.
- Krauthammer, T., Assadi-Lamouki, A., Shanaa, H.M. (1993). Analysis of Impulsively Loaded Reinforced Concrete Structural Elements – I. Theory. *Computers & Structures*, 48 (5), 851-860.
- Luccioni, B.M., Ambrosini, R.D., Danesi, R.F. (2004). Analysis of building collapse under blast loads. *Engineering Structures*, 26 (1), 63-71.
- Luo, X., Sun, W., Chan, S.Y.N. (2007). Impact resistance of high-strength fiber-reinforced concrete**.** *Magazine of Concrete Research*, 59 (3), 199-210.
- Muhamad, R., Ali, M.S.M., Oehlers, D.J., Sheikh, A.H. (2010). *Load-Sip Relationship of Tension Reinforcement in Reinforced Concrete Members*. Research Report, School of Civil and Environment Engineering, The University of Adelaide, Australia.
- Ngo, T., Mendis, P., Krauthammer, T. (2007). Behavior of ultrahigh-strength subjected to prestressed concrete panels blast loading. *Journal of Structural Engineering*, ASCE, 133(11), 1582-1590.
- Osteraas, J.D. (2006). Murrah building bombing revisited: A qualitative assessment of blast damage and collapse patterns. *Journal of Performance of Constructed Facilities*, ASCE, 20 (4), 30-335.
- Shi, Y., Hao, H., Li, Z. (2008). Numerical Derivation of pressure-impulse diagrams for prediction of RC column damage to blast loads. *International Journal of Impact Engineering*, 35 (2008), 1213-1227.
- Thompson, D., Brown, S., Mallonee, S., Sunshine D. (2004). Fatal and non-fatal injuries among US Air Force personnel resulting from the terrorist bombing of the Khobar Towers. *Journal of Trauma-Injury Infection and Critical Care*, 57 (2), 208-215.
- UFC-3-340-02. (2008). *Structures to Resist the Effect of Accidental Explosions.* US Department of the Army, Navy and Air Force Technical Manual.
- Weaver, W., Timoshenko, S.P. (1990). *Vibration Problems in Engineering*. Fifth Ed. Wiley, New York.
- Wu, C., Oehlers, D.J., and Day, I. (2009b). Layered Blast Capacity Analysis of FRP Retrofitted of RC Members. *Advances in Structural Engineering*, 12 (3), 435-449.

- Wu, C., Oehlers, D.J., Rebentrost, M., Leach, J., Whittaker, A.S. (2009a). Blast testing of ultra-high performance fiber concrete slabs and FRP retrofitted RC slabs. *Engineering Structures*, 31 (9), 2060-2069.

Table 1 Charge properties and slab models used in blast events for validation

Event No	Slab No	Charge mass (kg)	Standoff distance (m)	Scaled distance (m/kg$^{1/3}$)	Charge shape
6	D2B	14	1	0.4	cylindrical
7	D3B	8	1	0.5	cylindrical

Table 2 Quantification of the effects of the moment rotation relationship on P_{rmin}

Properties							**$Pr_{min}/P_{rmin,o}$**		
n bars	**k_τ**	**k_{yp}**	**$k_{yp}/k_{yp,o}$**	**k_{duc}**	**$k_{duc}/k_{duc,o}$**	**M/M_o**	**numer.**	**theor.**	**Error (%)**
5b	2.2	0.913	0.946	0.240	0.905	0.779	1.500	1.500	0.000
5b	1.25	0.991	1.026	0.269	1.017	0.676	1.430	1.418	0.870
5b	0.9	0.993	1.029	0.280	1.056	0.637	1.460	1.445	1.011
8b	1.25	0.966	1.001	0.266	1.003	0.888	1.120	1.122	0.166
5b	0.5	0.992	1.027	0.306	1.155	0.587	1.430	1.435	0.348
10b	1.25	0.966	1.000	0.265	1.000	1.000	1.000	1.000	0.000
15b	1.25	0.951	0.985	0.277	1.046	1.261	0.750	0.770	2.605
18b	1.25	0.953	0.987	0.302	1.142	1.363	0.660	0.651	1.359
		$k_{yp,power}$		**$k_{duc,power}$**				**average**	0.908
		0.29256		0.16817					

Table 3 Quantification of the effects of the moment rotation relationship on I_{min}

Properties						$\mathbf{I_{min}/I_{min,o}}$		
n bars	$\mathbf{k_\tau}$	$\mathbf{k_{yi}}$	$\mathbf{k_{yi}/k_{yi,o}}$	**W**	$\mathbf{W/W_o}$	**numer.**	**theor.**	**Error (%)**
5b	2.2	0.734	0.827	5.732	0.335	1.580	1.571	0.561
5b	1.25	0.969	1.091	8.632	0.505	1.440	1.471	2.139
5b	0.9	0.977	1.101	9.597	0.561	1.400	1.401	0.089
8b	1.25	0.890	1.003	13.756	0.804	1.090	1.117	2.456
5b	0.5	0.973	1.096	13.904	0.813	1.190	1.162	2.386
10b	1.25	0.887	1.000	17.110	1.000	1.000	1.000	0.000
15b	1.25	0.844	0.951	35.499	2.075	0.690	0.677	1.901
18b	1.25	0.849	0.956	69.907	4.086	0.480	0.484	0.800
			$\mathbf{k_{yi,power}}$				**average**	1.476
			1.0					

Table 4 Quantification of the effects of the depth of the member on P_{rmin}

					$P_{rmin}/P_{rmin,o}$		
Depth	$k_{yp}/k_{yp,o}$	$k_{duc}/k_{duc,o}$	M_u/M_{uo}	$(D/D_o)^{Dp,power}$	**theor.**	**numer.**	**Error (%)**
100	1.000	1.000	1.000	1.000	1.000	1.000	0.000
135	0.976	0.815	2.271	1.192	0.464	0.455	2.011
170	0.967	0.705	4.029	1.363	0.267	0.270	1.128
205	0.968	0.626	6.265	1.521	0.173	0.175	1.122
240	0.963	0.573	9.128	1.667	0.119	0.118	0.874
				$D_{p,power}$		**average**	1.284
				0.584			

Table 5 Quantification of the effects of the depth of the member on I_{min}

				$I_{min}/I_{min,o}$		
Depth	$k_{yi}/k_{yi,o}$	W/W_o	$(D/D_o)^{Di,power}$	**theor.**	**numer.**	**Error (%)**
100	1.000	1.000	1.000	1.000	1.000	0.000
135	0.976	1.531	1.447	0.645	0.650	0.740
170	0.967	2.036	1.922	0.477	0.490	2.599
205	0.968	2.428	2.420	0.391	0.380	2.797
240	0.963	3.047	2.938	0.313	0.315	0.576
			$D_{i,power}$		**average**	1.678
			0.616			

Table 6 Parameters of the control specimen

L_o	D_o	$M_{u,o}$	$M_{y,o}$	$\theta_{u,o}$	$I_{min,o}$	$P_{rmin,o}$
(m)	(mm)	(kNm/m)	(kNm/m)	(rad)	(kPa.ms)	(kPa)
2.07	100	215.2	191.4	0.0795	3550	340

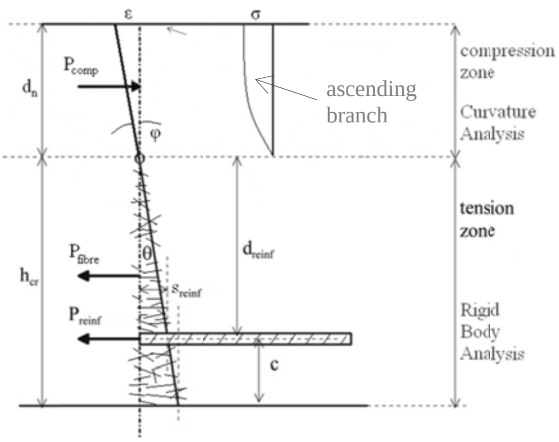

Figure 1 Moment rotation analysis

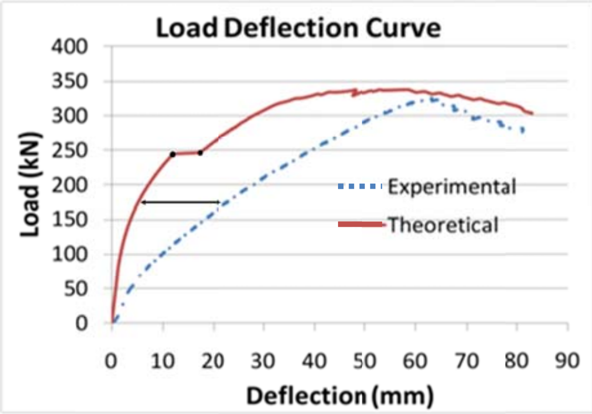

Figure 2 UHPC slab D2B load deflection relationship

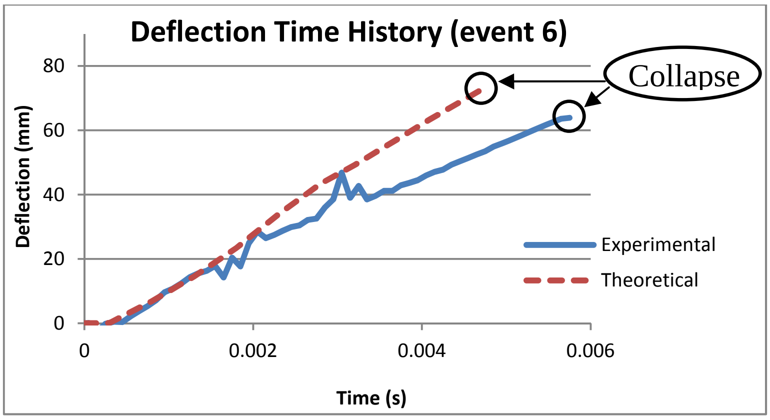

Figure 3 Deflection time history for event 6

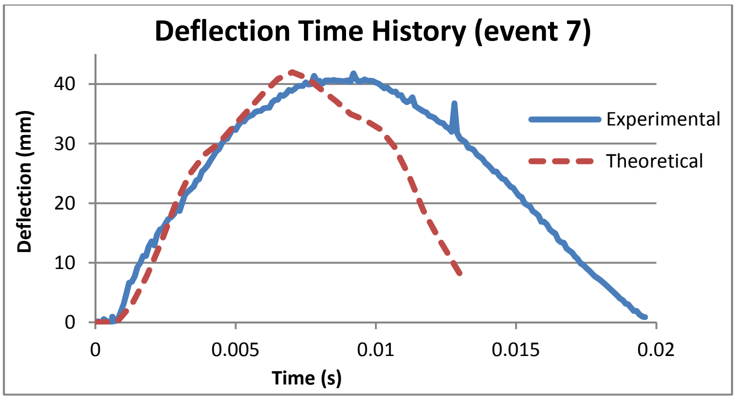

Figure 4 Deflection time history for event 7

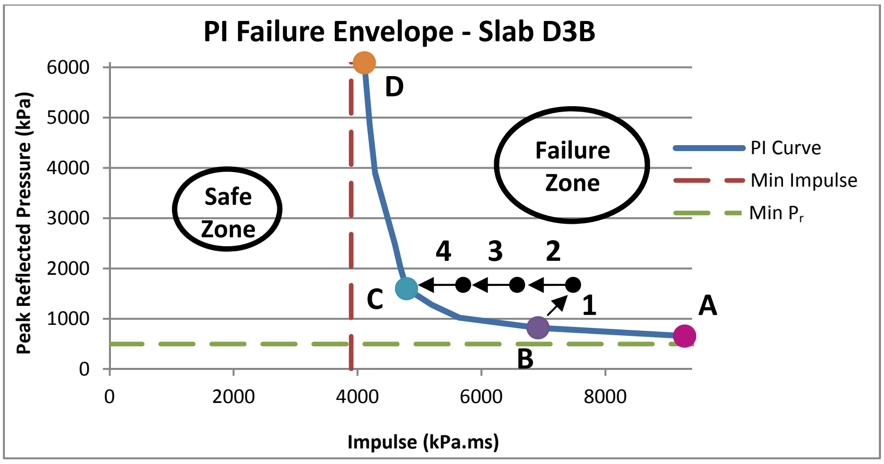

Figure 5 PI curve for slab D3B

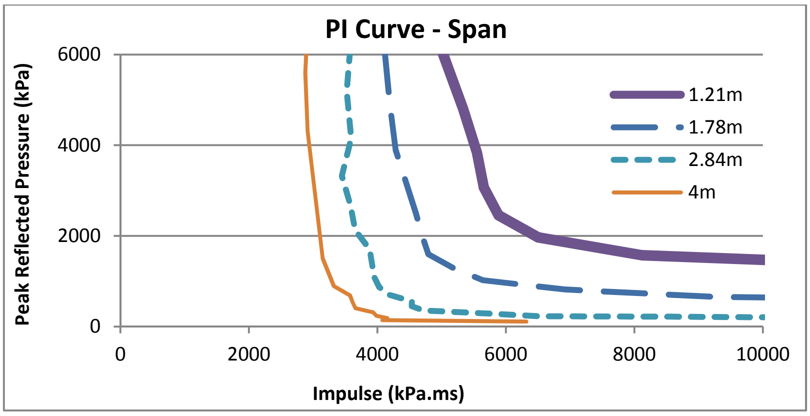

Figure 6 PI curves for slabs of varying spans

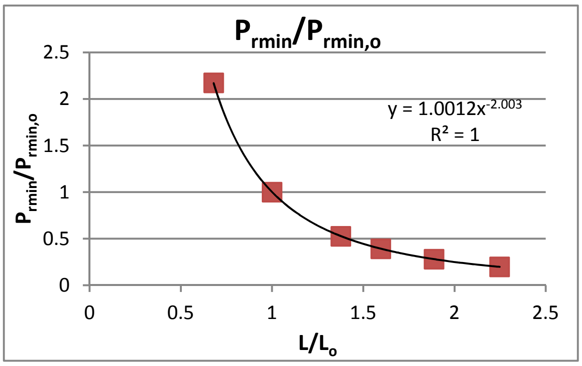

(a)

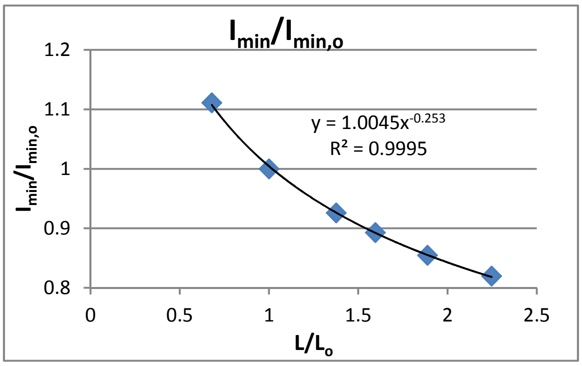

(b)

Figure 7 Effects of span on P_{rmin} (a) and I_{min} (b)

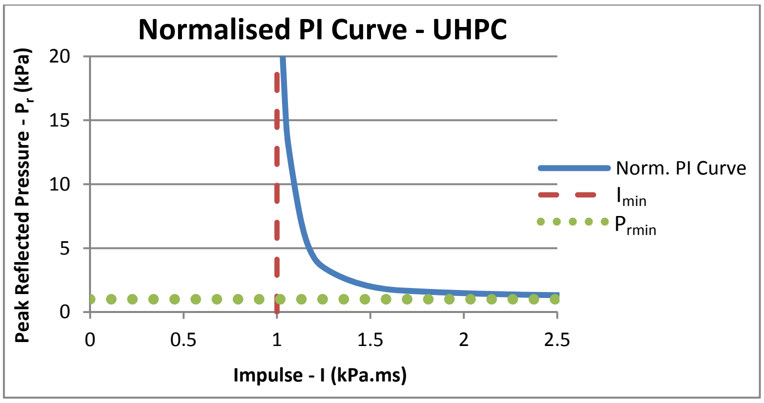

Figure 8 Normalized PI curve

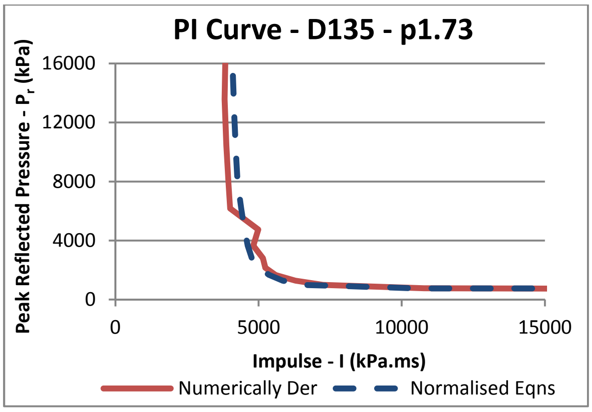

(a)

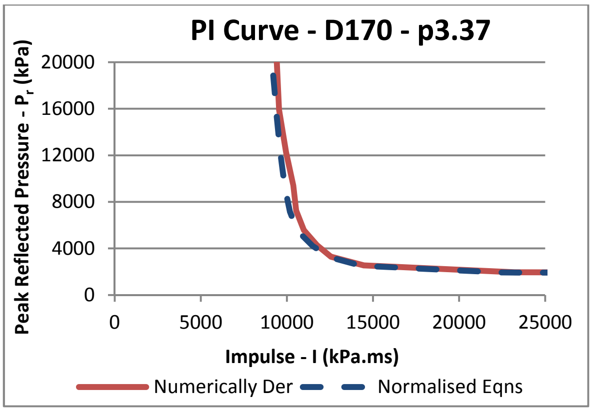

(b)

Figure 9 Numerically derived and theoretical PI curves for 2 separate specimens